J. Fluid Mech. (1993), *vol.* 255, *pp.* 597–620

On parasitic capillary waves generated by steep gravity waves: an experimental investigation with spatial and temporal measurements

By MARC PERLIN,[1] HUANJAY LIN[2] AND CHAO-LUNG TING[1]

[1] Department of Naval Architecture and Marine Engineering, University of Michigan, Ann Arbor, MI 48109, USA

[2] Department of Mechanical Engineering and Applied Mechanics, University of Michigan, Ann Arbor, MI 48109, USA

(Received 4 January 1993 and in revised form 6 May 1993)

An experimental investigation of steep, high-frequency gravity waves ($\sim$ 4 to 5 Hz) and the parasitic capillary waves they generate is reported. Spatial, as well as temporal, non-intrusive surface measurements are made using a new technique. This technique employs cylindrical lenses to magnify the vertical dimension in conjunction with an intensified, high-speed imaging system, facilitating the measurement of the disparate scales with a vertical surface-elevation resolution on the order of 10 μm. Thus, high-frequency parasitic capillary waves and the underlying gravity wave are measured simultaneously and accurately in space and time. Time series of spatial surface-elevation measurements are presented. It is shown that the location of the capillary waves is quasi-stationary in a coordinate system moving with the phase speed of the underlying gravity wave. Amplitudes and wavenumbers of the capillaries are modulated in space; however, they do not propagate with respect to the gravity wave. As capillary amplitudes are seen to decrease significantly and then increase again in a recurrence-like phenomenon, it is conjectured that resonance mechanisms are present. Measured surface profiles are compared to the theories of Longuet-Higgins (1963) and Crapper (1970) and the exact, two-dimensional numerical formulation of Schwartz & Vanden-Broeck (1979). Significant discrepancies are found between experimental and theoretical wavetrains in both amplitude and wavenumber. The theoretical predictions of the capillary wave amplitudes are much smaller than the measured amplitudes when the measured phase speed, amplitude, and wavelength of the gravity wave are used in the Longuet-Higgins model. In addition, this theory predicts larger wavenumbers of the capillaries as compared to experiments. The Crapper model predicts the correct order-of-magnitude capillary wave amplitude on the forward face of the gravity wave, but predicts larger amplitudes on the leeward face in comparison to the experiments. Also, it predicts larger capillary wavenumbers than are experimentally determined. Comparison of the measured profiles to multiple solutions of the stationary, symmetric, periodic solutions determined using the Schwartz & Vanden-Broeck numerical formulation show similar discrepancies. In particular, the assumed symmetry of the waveform about crest and trough in the numerical model precludes a positive comparison with the experiments, whose underlying waves exhibit significantly larger capillaries on their forward face than on their leeward face. Also, the *a priori* unknown multiplicity of numerical solutions for the same dimensionless surface tension and steepness parameters complicates comparison. Finally, using the temporal periodicity of the wave field, composite images of several successive wavelengths are constructed

from which potential energy and surface energy are calculated as a function of distance downstream.

1. Introduction

Steep gravity waves are known to generate capillary waves on their forward faces. This is apparently due to the large curvature along the crests where surface tension becomes locally important. These waves may be referred to as parasitic capillary waves. Parasitic capillary waves are important for several reasons, three of which are: (i) as a mechanism for extracting energy from the primary gravity wave through viscous energy dissipation at short scales, (ii) as a mechanism for generating surface roughness at wavelengths which scatter electromagnetic radiation (and thus are germane to the interpretation of remotely sensed information), and (iii) as a source of near-surface vorticity as shown by Longuet-Higgins (1992). Surprisingly little information is available on these waves of disparate scales, presumably due to the analytical/numerical, as well as experimental, difficulties involved.

Analytical/numerical solutions of the generation of parasitic capillary waves by steep gravity waves have been formulated by Longuet-Higgins (1963), Crapper (1970), Schwartz & Vanden-Broeck (1979), Chen & Saffman (1979, 1980, 1985), Ruvinsky & Freidman (1981, 1985), and Ruvinsky, Feldstein & Freidman (1991). Longuet-Higgins (1992) has discussed the generation of near-surface vorticity by the steep gravity wave and the contribution to this vorticity by the capillary waves. Experimental investigations have been carried out by Cox (1958), Miller (1972), Chang, Wagner & Yuen (1978), and Yermakov *et al.* (1986); however, these investigators reported surface slope as a function of time, only. Neither surface-elevation measurements, nor phase-speed measurements, nor spatial-dissipation measurements of the wavetrains were presented. Herein, using a newly developed system, extremely accurate measurements of surface *elevation* are presented. Resolution and accuracy of the vertical measurements are shown to be on the order of 10 μm. Temporal series of spatial surface elevation are presented for cyclic frequencies of 4.21 and 5.26 Hz, two of the three frequencies reported in Chang *et al.* (1978). (Spatial series of temporal surface elevation are also available.) From these data, phase speeds are calculated. In addition, potential energy and surface energy as a function of distance downstream is given. Significant differences are shown to exist between theory and experiment.

In §2, the theories of Longuet-Higgins and of Crapper are reviewed. (Presumably, lacking experimental results of surface elevation with which to compare, neither theorist presented surface profiles. Thus, their equations are presented. The corresponding surface profiles are shown and discussed in §4.) Also, the formulation of Schwartz & Vanden-Broeck is presented. Section 3 discusses the measurement technique, its accuracy, and the laboratory facility. Experimental results are presented and compared to the theoretical/numerical solutions in §4. Conclusions are given in §5.

2. Analytical/numerical theories

2.1. *Theory of Longuet-Higgins* (1963)

A brief discussion of the theory of Longuet-Higgins (1963) is now given. (The equations presented are limited to those solved to obtain the surface profile.) The theory is based on a perturbation technique which assumes that at zeroth order a

nonlinear gravity wave is present with waveform given by the solution of Davies (1951) as

$$z_0 = x_0 + \mathrm{i}y_0 = \frac{1}{c}\int_0^{\chi} \frac{\mathrm{d}\chi}{(1 - A\,\mathrm{e}^{-\mathrm{i}m\chi})^{\frac{1}{3}}} = \frac{1}{c}\int_0^{\phi} \frac{\mathrm{d}\phi}{(1 - A\,\mathrm{e}^{-\mathrm{i}m\phi})^{\frac{1}{3}}} \quad \text{(on the free surface)}, \quad (1)$$

where $\chi = \phi + \mathrm{i}\psi \quad (\psi = 0, \text{ on the free surface}),$

$$m = lg/c^3, \quad 1 < l < \tfrac{3}{2}, \quad 0 < A < 1.$$

At first order, the capillary wavetrain is given by the expression

$$z_1 = x_1 + \mathrm{i}y_1 = \frac{1}{c}\int_0^{\chi} \frac{\mathrm{d}\chi}{\mathrm{e}^{\tau_1 - \mathrm{i}\theta_1}} = \frac{1}{c}\int_0^{\phi} \frac{\mathrm{d}\phi}{\mathrm{e}^{\tau_1 - \mathrm{i}\theta_1}} \quad \text{(on the free surface)}, \quad (2)$$

where

$$\tau_1 - \mathrm{i}\theta_1 = \begin{cases} -\mathrm{i}b\,\mathrm{e}^{-\mathrm{i}((\rho c)/T)(\alpha + \mathrm{i}\beta)} & (\alpha < 0) \\ 0 & (\alpha > 0) \end{cases} \quad \text{(on the free surface, } \psi = \beta = 0)$$

$$b = -4\int_0^{\infty} \frac{\partial \tau_0}{\partial \psi} \cos\left(\frac{\alpha \rho c}{T}\right) \mathrm{d}\phi, \quad \alpha \approx \int_0^{\phi} \mathrm{e}^{\tau_0}\,\mathrm{d}\phi$$

with $$\mathrm{e}^{\tau_0} = (1 - 2A\cos m\phi + A^2)^{\frac{1}{6}},$$

$$\frac{\partial \tau_0}{\partial \psi} = -\frac{m\delta}{3(\delta^2 + m^2\phi^2)}, \quad \text{and} \quad \delta = 1 - A.$$

Values for b, $\partial\tau_0/\partial\psi$, and α are near-crest approximations as given by Longuet-Higgins. In addition, to model viscous dissipation, the imaginary part of the solution to (2) is multiplied by

$$y_1 = y_1\left(1 - \exp\left(\frac{-4\rho^2\nu}{T^2}\int_0^{\phi} (c\,\mathrm{e}^{\tau_0})^2\,\mathrm{d}\phi\right)\right).$$

Here, the subscripts refer to the zeroth- and first-order solutions; z is a complex coordinate with x and y representing the horizontal and vertical coordinates, respectively. The wave profile is obtained by superposition of z_0 and z_1. Also, x is positive to the right and y is positive directed upward from the water surface; χ is the complex potential with ϕ the velocity potential and ψ the stream function. The phase speed of the gravity wave is denoted by c while A is a parameter related to the wave amplitude of the gravity wave. $A = 1$ corresponds to gravity-wave breaking. The parameter l corresponds to the wavelength of the gravity wave, g is the acceleration due to gravity, ρ is the mass density, ν is the kinematic viscosity, and T is the surface tension. Equations (1) and (2) are integrated to obtain the gravity wave profile and the capillary wavetrain, respectively. The sum of these waves yields the water surface. Solutions are given and compared to experiments in §4.

2.2. *Theory of Crapper* (1970)

The theory of Crapper (1970) used the same underlying nonlinear gravity wavetrain as Longuet-Higgins at zeroth order; however, the solution at first order incorporated the exact solution of Crapper (1957) for the capillary waves. A nonlinear, ordinary

differential energy equation was given in terms of C, an integration constant, as follows:

$$\frac{-\rho U^3}{(T^2-C\rho U^2)^{\frac{1}{2}}}\frac{\mathrm{d}C}{\mathrm{d}s} = \left| Tc\sin\theta\frac{\partial U}{\partial\psi}\right| - \frac{4\nu\rho^2U^4\bar{k}}{T}(3\bar{k}^2-1)(\bar{k}^2-1). \tag{3}$$

Here, U and θ are the surface-particle velocity magnitude and direction, respectively, in the gravity wave, and $\bar{k}$ is a non-dimensional capillary wavenumber. These are defined as

$$U = c(1+A^2-2A\cos m\phi), \quad \theta = \tfrac{1}{3}A\tan^{-1}\left(\frac{-A\sin m\phi}{1-A\cos m\phi}\right), \quad \text{and} \quad \bar{k} = \frac{T}{(T^2-C\rho U^2)^{\frac{1}{2}}}.$$

$\partial U/\partial\psi$ is given by

$$\frac{\partial U}{\partial\psi} = -\frac{cmA(\cos m\phi - A)}{3(1-2A\cos m\phi + A^2)^{\frac{5}{6}}}.$$

The solution of (3) along the curvilinear coordinate, s, where $\mathrm{d}s$ is the length element along the zeroth-order solution of the free surface, gives the capillary wavetrain. Since $\bar{k}$ is a continuous function of ϕ, the solution of the above equations is difficult. To simplify the solution, the number of capillary waves along the gravity wave profile is determined (as a function of ϕ) using the following equation:

$$n = \frac{1}{2\pi}\int_0^{\phi}\frac{\rho U}{(T^2-C\rho U^2)^{\frac{1}{2}}}\mathrm{d}\phi.$$

Between integer values of n, then, using the appropriate $\bar{k}$ for each capillary wavelength, (3) is solved using Euler's method.

2.3. *The numerical theory of Schwartz & Vanden-Broeck* (1979)

A review of the numerical treatment of the exact, two-dimensional water wave problem including surface tension and gravity as given by Schwartz & Vanden-Broeck is presented. They assumed a two-dimensional, infinite-depth fluid which is inviscid, incompressible, and of constant density. In addition, the assumption of irrotational flow is made. The waves are assumed of permanent-form and symmetric about a vertical axis through crest and trough. With these assumptions, a complex physical coordinate, $z = x+\mathrm{i}y$, a complex potential, $\chi = \phi+\mathrm{i}\psi$, and a complex velocity, $q = \mathrm{d}\chi/\mathrm{d}z = u-\mathrm{i}v$ are defined. In a system of coordinates moving at the constant phase speed, c, the kinematic condition is identically satisfied while the dynamic condition on the free surface is

$$\tfrac{1}{2}qq^* + gy + T/\rho R = \tfrac{1}{2}c^2, \tag{4}$$

where the variables are defined as before, the asterisk represents the complex conjugate, and R is the surface radius of curvature with positive defined with centre in the fluid. Three dimensionless parameters are chosen: a dimensionless surface tension parameter (following Wilton's original work), $\kappa = (k^2T)/(\rho g)$; a dimensionless wave-speed parameter, $\mu = (k/g)c^2$; and a dimensionless measure of wave steepness, $\epsilon = (y(0)-y(\pi/k))/(2\pi/k)$, whose choice is unclear for multi-crested steep waves. ($\kappa = 1/n$ represents nth-harmonic resonance for the weakly nonlinear theory.) Using the first two dimensionless parameters, (4) becomes

$$\tfrac{1}{2}\hat{q}\hat{q}^* + \hat{y} + \kappa/R = \tfrac{1}{2}\mu, \tag{5}$$

where the circumflexes denote dimensionless variables. Next the flow is separated into a uniform part and a wave part using the transformation $\hat{z} = \mu^{-\frac{1}{2}}\hat{\chi} + \hat{\zeta}$. Periodicity is

imposed using the transformation $\hat{\chi} = \hat{\phi} + \mathrm{i}\hat{\psi} = \mathrm{i}\mu^{\frac{1}{2}} \log \zeta$, where $\zeta = r\,\mathrm{e}^{\mathrm{i}\theta}$ and $r = 1$ is the surface. Exploiting the assumed symmetry of the permanent-form wave, the surface condition is expressed in terms of the unknown function, $\hat{z} = \hat{z}(\hat{x}(\theta), \hat{y}(\theta))$, as

$$\frac{\hat{y}}{\mu} + \frac{1}{2}\left(\frac{1}{\hat{x}'^2 + \hat{y}'^2} - 1\right) + \frac{\kappa}{\mu}\left(\frac{\hat{x}'\hat{y}'' - \hat{y}'\hat{x}''}{(\hat{x}'^2 + \hat{y}'^2)^{\frac{3}{2}}}\right) = 0, \tag{6}$$

where the primes denote differentiation with respect to θ. Schwartz & Vanden-Broeck fix (ϵ, κ) and seek solutions in terms of μ. A Newton–Raphson technique is used to solve the set of nonlinear algebraic equations obtained by finite differencing (6).

In this paper multiple solutions are found as in Schwartz & Vanden-Broeck. That is, for given values of (ϵ, κ), several numerical solutions are found with different values of the speed parameter, μ. In the results presented herein, sixty points are used to define the surface along a half-wavelength with double precision, 32-bit arithmetic, and a convergence criterion of 10^{-6} for each point. The wave profile determined numerically in a straightforward manner beginning with an initially sinusoidal profile is termed the 'naturally' occurring waveform by Schwartz & Vanden-Broeck and this terminology is used herein. One straightforward technique and one 'bootstrap' technique similar to that described by Schwartz & Vanden-Broeck are used to search for multiple solutions. The bootstrap search technique is employed for the 5.26 Hz wavetrain, only. (For the 4.21 Hz experiments, the straightforward technique is used and only the naturally occurring solution is presented.) The first technique begins with a sinusoidal input with fixed values of $(\epsilon, \kappa) = (0.06727, 0.06275)$ as determined from the experiments and an initial guess of μ varying from 1.0 to 2.0 in 0.01 increments. Three solutions are determined. (See §4 for a discussion of the three profiles determined.)

Next, the bootstrap technique is employed as none of these three solutions had an appropriate number of short waves present nor did they have a phase-speed parameter corresponding to that measured experimentally. Since the experimental wavetrain had about seven short waves present on its half-wavelength, $\kappa = 0.07143$, the numerical simulation begins with this initial value of κ. It is hoped that by slowly varying κ, a profile with the corresponding number of short waves present could be determined. Also, a profile with a phase-speed parameter, μ, approximately equal to the experimental value of 1.2124 is sought. Beginning with an initial value of $\mu = 1.0$ and a sinusoidal wavetrain with steepness $\epsilon = 0.06727$, a solution is determined. Then, κ is decreased by 1/99th of the difference between the experimental value of κ and the initial value of κ (or -0.00008768), the convergent waveform is used as the initial waveform, and the convergent value of μ is used as the initial guess. Upon determining a convergent solution, this process is repeated until $\kappa = 0.06275$ is reached. At this point, starting values of $(\epsilon, \kappa) = (0.06727, 0.07143)$ and a sinusoidal wavetrain with an initial guess of $\mu = 1.01$ are used. The process is repeated in its entirety through an initial value of $\mu = 2.0$. In this manner, 10000 solutions are sought in order to approach $\kappa = 0.06275$ from larger values of κ and several values of μ. No additional convergent solutions are found for $(\epsilon, \kappa) = (0.06727, 0.06275)$.

3. Non-intrusive surface-profile measurement system and laboratory facility

Components of the non-intrusive surface-profile measuring system are a Spectra-Physics 164, 2 W, Argon–Ion laser; attendant optics (a spherical and a cylindrical lens) which shape the beam into a laser sheet with its beam waist at the mean water level;

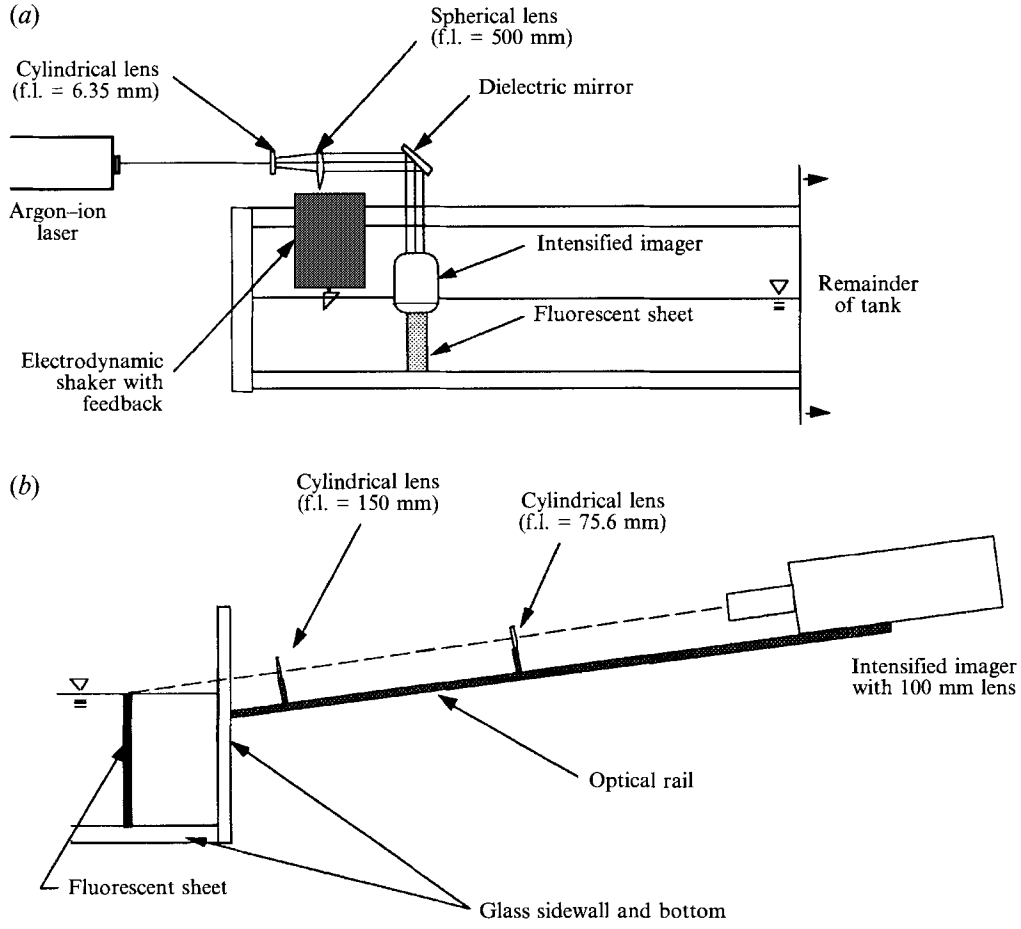

FIGURE 1. Schematic of non-contact measuring system. (*a*) Elevation view along longitudinal section. (*b*) Elevation view along transverse section.

a Kodak Ektapro high-speed, 8-bit video system with intensified imager with gating to 1 μs and framing to 12 kHz; and attendant optics to magnify the vertical image by a factor of about 7 to 8 (two cylindrical, convex lenses). As this system is new and unique, a discussion of the components, optics, capabilities, and calibration is presented. A description of the remainder of the gravity–capillary wave laboratory follows.

A schematic of the non-contact measurement system is shown in figure 1. Part (*a*), an elevation view of the longitudinal section of the wave tank, shows a schematic of the laser-sheet generating system. A cylindrical lens with a focal length of 6.35 mm is used to expand the beam in one direction, only. A spherical lens with a focal length of 500 mm focuses the beam, after it is redirected by a dielectric mirror, to a narrow waist coincident with the quiescent water surface. The thickness of the laser sheet at the quiescent water/air interface is less than ~ 0.5 mm. Rhodamine-B dye is added to the water as the fluorescing agent for the chosen 514.5 nm wavelength light of the Argon–Ion laser. The rated power output of the laser is 2 W. The power output of the 514.5 nm wavelength is approximately 0.6 W.

Figure 1 (*b*), an elevation view of the transverse section of the wave tank, shows the physical set-up of the intensified imager and magnification and measurement optics. In figure 2, a ray-tracing diagram of the magnification/imaging optics is presented.

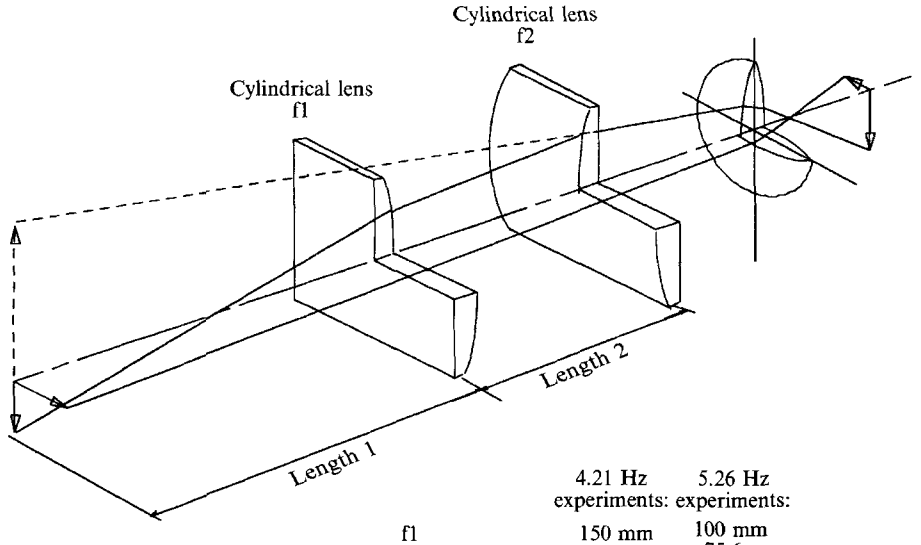

	4.21 Hz experiments:	5.26 Hz experiments:
f1	150 mm	100 mm
f2	75.6 mm	75.6 mm
Theoretical length 1	336 mm	190 mm
Theoretical length 2	338 mm	277 mm
Actual length 1	339 mm	199 mm
Actual length 2	360 mm	293 mm
Camera lens setting	100 mm	80 mm

FIGURE 2. Ray-tracing diagram of the magnification/imaging optics.

	4.21 Hz experiment	5.26 Hz experiment	System capabilities
Vertical resolution (mm/pixel)	0.0446	0.0470	0.0050
Horizontal resolution (mm/pixel)	0.349	0.351	0.039
Temporal resolution (μs)	50	50	1
Actual vertical exaggeration	7.8	7.5	7.8

TABLE 1. Experimental resolutions and system capabilities

Convex lenses with focal lengths and separation distances as shown in the figure are used. The configuration is chosen to maximize the useful area of an image with the constraint that an entire wavelength of the underlying gravity wave is visible. Also show in figure 2 are the theoretical distances required to give a vertical exaggeration (i.e. the ratio of the enlargement of the vertical dimension to that of the horizontal dimension) of 8.0 along with the actual lengths used. (For the vertical exaggeration, see table 1.)

The imaging system is a Kodak Ektapro CID (charge-injection device) intensified imager and controller coupled to an Ektapro EM 1012 processor (i.e. a controller and recorder). It is capable of framing rates to 12 kHz (83.3 μs) and gating (shutter) rates as fast as 1 MHz (1 μs). A typical illumination level is 1.5 lux at a 1000 Hz framing rate with 1 μs gating and the maximum gain. At present, the unit is capable of recording 400 frames (in RAM), expandable to 4800 frames. The image is composed of 239 horizontal pixels by 192 vertical pixels. Pixels are undistorted in the two imaging dimensions.

Once a set of 400 (or less) images is stored in RAM in the Ektapro 1012, it is downloaded to a Macintosh IIfx via a standard GPIB interface. Various programs

written in LabVIEW control the type of images transferred and recorded. For example, a time series at a spatial point is obtained by stringing together a column of data from each full-frame of the temporal series of spatial images to compose a new image. This facilitates comparisons with other investigations which present temporal measurements at spatial locations. Sequential spatial series over time are displayed using various imaging software (see §4). From these images, phase speeds and vertical and horizontal coordinates of the surface profiles are gleaned. Thus, spatial evolution of the profiles is recorded.

The vertical and horizontal resolutions are determined using precision Ronchi rulings with 4 cycles/mm and 2 cycles/mm, respectively. Using the known line spacings of the Ronchi rulings and the corresponding number of pixels obtained from the recorded images (using vertical and horizontal reticles available in the Ektapro), the resolutions are computed. In table 1, the resolutions of each experiment as well as the system capabilities are presented. A 100 mm focal-length lens and a 70–210 mm focal-length zoom lens is used in the 4.21 and 5.26 Hz experiments, respectively. The theoretical vertical exaggeration is 8.0. The vertical exaggeration realized is 7.8 and 7.5 in the 4.21 and 5.26 Hz experiments, respectively. In the experiments reported, the vertical resolution is limited by the desire to capture entirely, in each image, the crest-to-trough region.

An indication of the accuracy of the images is presented in figure 3. Spherical aberration is avoided as much as possible by using the central region of the cylindrical lenses. The calibration targets are placed in the same plane as the eventual location of the laser sheet. Its horizontal midline is located at the eventual location of the mean water level. Figure 3(*a*) shows a recorded image of the precision, horizontally ruled 4 cycles/mm lines used to calculate vertical resolution and show distortion. The camera lens is set to 200 mm for these calibration images, only. The duty cycle is 0.5. Slight distortion is apparent. Figure 3(*b*) shows a recorded image of the precision, vertically ruled, 2 cycles/mm lines used to calculate horizontal resolution and show distortion. A slight 'pin-cushion' effect is seen, particularly at this image's extremities; however, owing to the location of the distortion (typically, our surface profiles do not extend into the corner regions), it is decided that geometric-distortion correction is unwarranted. In figure 3, the vertical exaggeration is about 7.3.

An additional discussion is necessary at this junction; namely, in order to obtain spatial information over several of the long wavelengths (which is necessary for the dissipation calculation) without sacrificing resolution, the following procedure is used. After demonstrating that the wave field is temporally periodic (see figure 4 and the discussion in §4), as are all of the experiments discussed herein, the trigger which signals the imager to begin recording is coupled to a specific phase of the wave-generator signal. The phase is arbitrarily chosen as the zero up-crossing point of the wave-generator signal. (This is done simply by having the computer output two D/A signals, one a sinusoidal signal which is sent to the electrodynamic shaker, the other a square wave with TTL voltage which is sent to the Ektapro.) This ensures that at various spatial locations of the imager, the phases of all of the images are identical for a particular frame number. Thus, images with the same frame number can be placed adjacent to each other to form an image of the wave field as many gravity wavelengths long as desired. Vertical control is accomplished by positioning the imager so that the quiescent water level is at the same row-of-pixels location in each set-up. Horizontal control, which ensures that when the images are aligned there is neither overlap nor gap, is accomplished by including in the image a scale which is of sufficient length to span the desired measurement distance. In addition, redundant horizontal control is

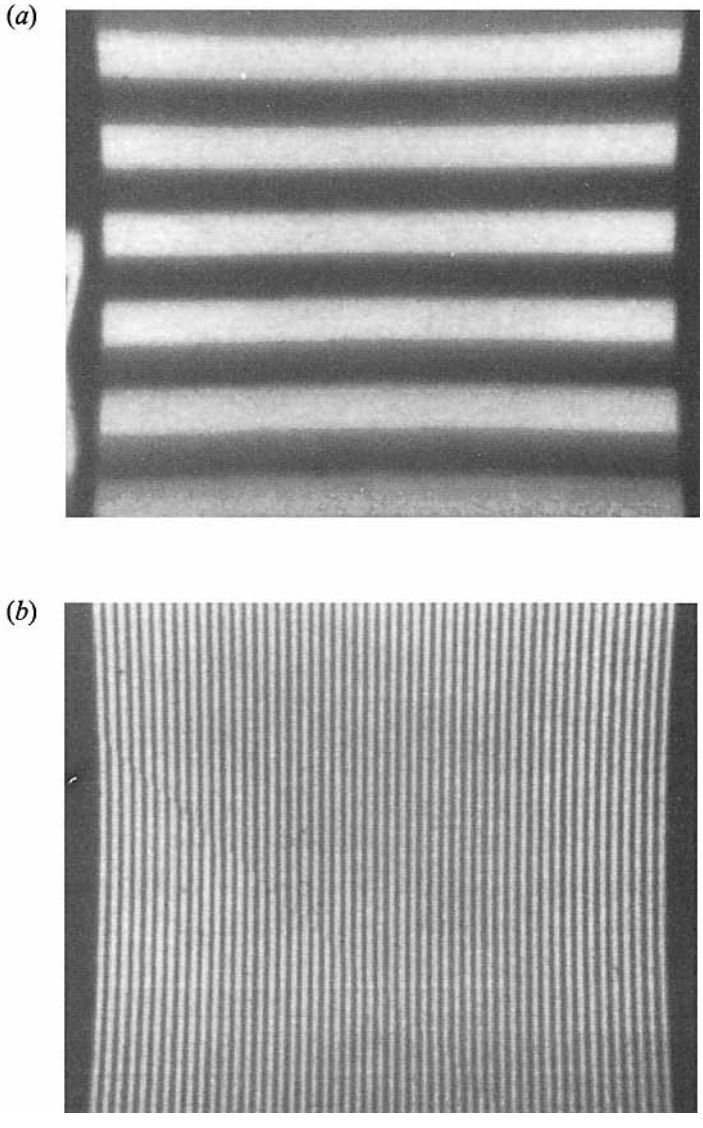

FIGURE 3. Recorded images of precision rulings used to determine accuracy and resolution. (*a*) Horizontal lines of a 4 cycle/mm precision Ronchi ruling used for vertical calibration. (*b*) Vertical lines of a 2 cycle/mm precision Ronchi ruling used for horizontal calibration. (Note the slight 'pin-cushion' effect.)

afforded by precisely measuring the placement of the imager. Using this alignment technique, there is the possibility of $\pm$one pixel error in each direction. A final check on the entire procedure is that the transition between adjacent images is smooth. That this is, indeed, the case is shown in §4.

The remaining laboratory facility consists of five subsystems: wave tank; wave maker and attendant electronics; wave-maker signal generation and data acquisition system; *in-situ* wave gauges and attendant electronics; and water treatment system. (See Perlin & Ting 1992 for a discussion of the laboratory.) Glass walls, separated by 71 cm, form a 240 cm channel downstream of the wave maker. The water depth is approximately 14 cm (deep water according to the linear wave theory for the

frequencies reported). The wave maker consists of an Unholtz-Dickie electrodynamic shaker Model 20 with a model TA100-20 amplifier; an aluminium right-angle-wedge wave paddle; and a feedback displacement transducer, Kaman model KD2300-10CU. The paddle dimensions are 5.03 cm vertical by 3.37 cm horizontal. Under static conditions, the wave paddle is immersed about 3.2 cm. The command signal (shaker digital-to-analog signal) is generated at 3000 Hz and data acquisition is accomplished using a Macintosh IIfx computer enhanced with National Instruments' LabVIEW software and data acquisition hardware packages. Prior to digitization, output signal to the wave maker and feedback signal from the displacement transducer are filtered using two Krohn-Hite model 3342 analog filters with a cut-off frequency of 250 Hz. These signals are monitored to ensure that the wave-maker position as a function of time is essentially the same as the desired position. The water treatment system includes a 5 μm particulate pre-filter, a de-ionization tank, a carbon adsorption phase, and a 0.2 μm particulate final filter. The wave tank and paddle are scrubbed before and after each use with ethyl alcohol. Static surface-tension measurements using a CSC-DuNoüy tensiometer are made routinely and agree with accepted values for clean water at room temperature; however, it is well-known that the presence of surface-active agents does not necessarily cause a significant change in static, surface-tension measurements. Thus, the presence of these contaminants cannot be entirely ruled out.

4. Results

In this section, using time series of spatial images, it is shown that the parasitic capillary waves are quasi-stationary with respect to a coordinate system fixed to the gravity wave. That is, they are formed primarily on the front face of the crest and along the trough of the gravity wave and are modulated in amplitude and wavelength, but do not propagate with respect to the gravity wave. This suggests that the capillary waves and the gravity waves are resonating, in some sense, as there is an exchange of energy as a particular capillary wave amplitude varies in space as the wave system propagates. The capillaries *emerge* from the smooth surface along the gravity wave, rather than propagating to their eventual quasi-stationary location.

Further, comparison is made to the theories of Longuet-Higgins and of Crapper and to the numerical solutions of Schwartz & Vanden-Broeck. Using the steepness of the experimental surface profile as input to the theories, the Longuet-Higgins theory substantially underpredicts the measured amplitudes of the capillaries as well as their wavelengths. The Crapper theory predicts the correct order of the measured capillary amplitudes on the forward face of the gravity wave, but overpredicts these amplitudes on the leeward face. Also, it underpredicts the measured wavelengths. Using the experimentally measured/computed values of (ϵ, κ), multiple numerical solutions are found (i.e. convergent solutions with different values of μ) using the Schwartz & Vanden-Broeck formulation. These solutions are presented and discussed. In addition to disagreement between amplitudes and wavenumbers of the short waves, it is found that the phase speed of the wavetrain is underpredicted. That is, no numerical solutions are determined with a value of μ which corresponds to the experiments. Processes neglected in the numerical formulation which are known to alter the phase speed do not account for the increase in phase speed, as they all cause a decrease. More likely is the possibility that the waveform with an appropriate μ-value is simply not found, or/and the slight distortion in the images (see figure 3) is sufficient to alter the measured phase speed (accounting for an approximate 4% difference). Finally, spatial values of potential and surface energies of the wave profiles are presented. The spatial series of

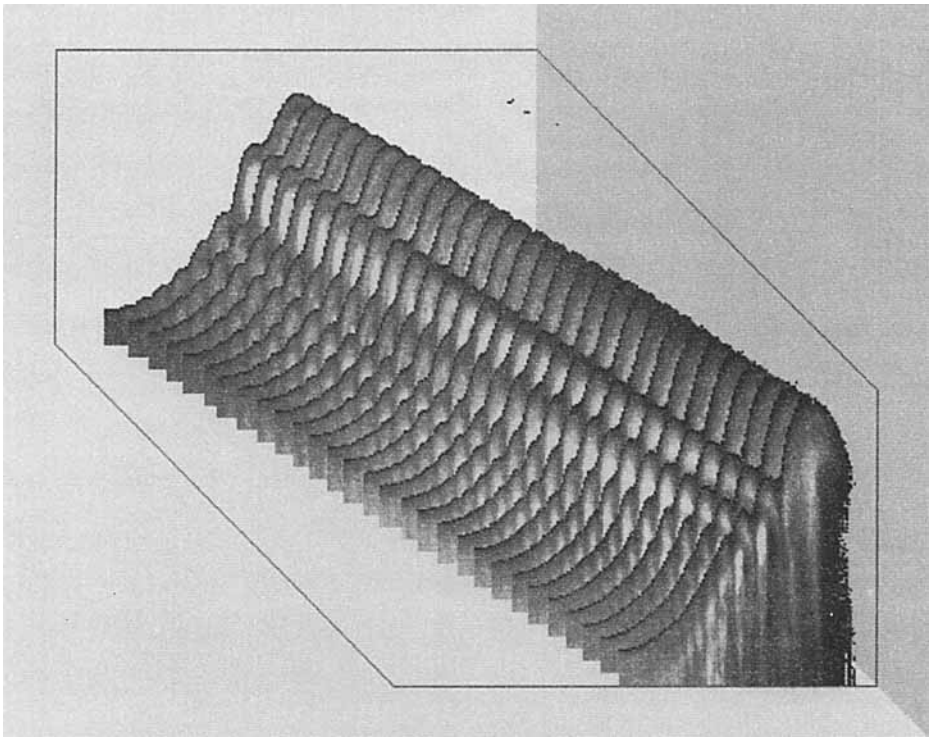

FIGURE 4. Time series of the 5.26 Hz wave profile showing about one-half wavelength of each image spaced 3 ms apart. The crest of the image in the foreground is located 0.5 wavelengths downstream of the wave maker.

surface elevation spanning several wavelengths required for these calculations are produced using the previously discussed triggering scheme to properly synchronize the snapshots of a temporally periodic signal to the zero up-crossing phase of the wave maker signal.

4.1. *The 5.26 Hz experiments*

Throughout the discussion of the images, the image separation distances are referenced to the image centres and are chosen so that slightly more than a complete wavelength is visible in an image, and thus adjacent images overlap slightly. These distances are measured from the quiescent water-surface's intersection with the wave paddle. In the figures, the wave is propagating from right to left with profiles shown at 3 ms intervals. The data are recorded at 1 ms intervals; however, showing all images recorded renders features more difficult to see. Time series, with all images present, are checked to ensure that no losses of significant features occur.

In figure 4, a time series of spatial data is presented which extends over one-half of a temporal wave period. For clarity, each of the images in the sequence shows about one-half of the spatial image including the forward face of the gravity wave. These waveforms are recorded 7.1 cm downstream (to the image centre). Thus, the first wave crest is located about one-half of a linear-theory wavelength from the wave maker. Clearly, these waves are evolving; however, note that a line connecting the crests of the gravity wave and another line connecting the first troughs along the forward face of the gravity wave are parallel. Thus, the location of the first parasitic capillary crest is fixed relative to the gravity wave crest. The amplitude of this first capillary is being

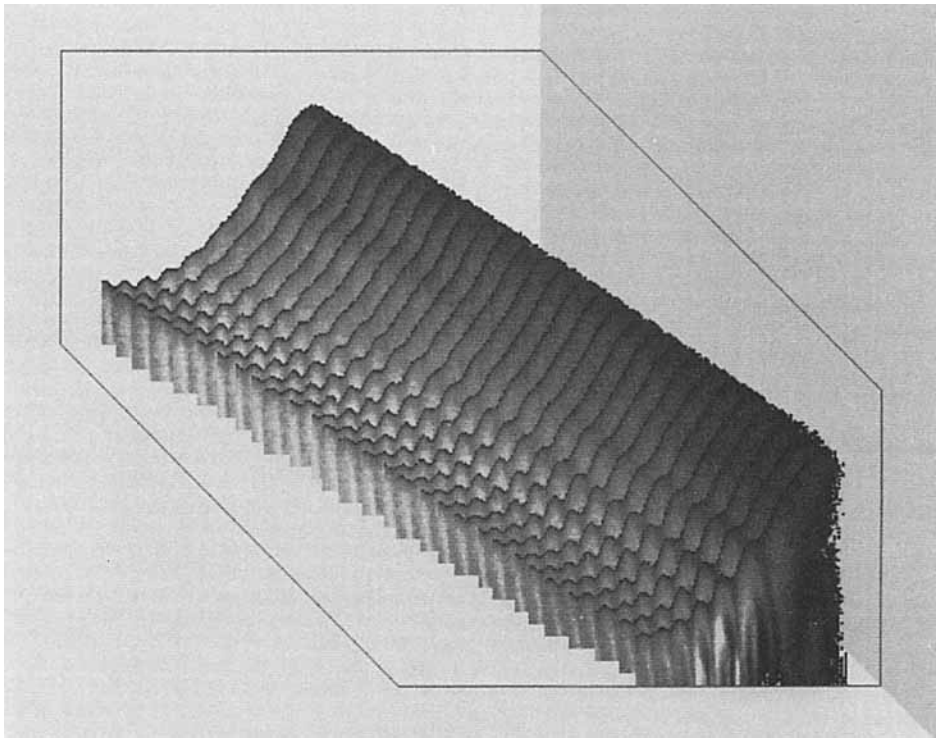

FIGURE 5. As figure 4 but the crest of the image in the foreground is located 1.5 wavelengths downstream of the wave maker.

modulated, as is its wavelength. Alternate views of the time series, as viewed from above, and comparisons of individual profiles show that the wavelengths are modulated about some mean wavelength. Therefore, it is mostly the amplitude modulation that causes the capillary wavelengths, especially the second capillary crests, to appear to be changing significantly. In the first profile, it is seen that three capillary crests are present on the half-profile, while only one-half wavelength downstream seven crests are seen. Note that these crests emerge from the gravity wave rather than propagating down the gravity wave's forward face. (This is consistent with the notion of a stationary capillary wavetrain in the moving coordinate system; however, the close proximity to the wave maker and the absence of capillaries travelling down the forward face of the gravity wave suggest that the physical argument that the capillaries are due to increased pressure due to increased surface curvature (which necessitates a transient period during which the capillaries are establishing the stationary situation) is suspect or that the transience occurs extremely quickly.) It is possible that the wavetrain of capillaries exists but that its amplitudes are too small to be seen and that its presence is due to increased pressure in the gravity wave crest due to the local surface curvature. However, it is clear that their spatial growth occurs due to energy exchange with the underlying gravity wave (through a possible resonance) and not through the propagation of capillary waves relative to the gravity wave.

Figure 5 is a time series of spatial profiles with the centre of the imaging system located two wavelengths downstream. The other parameters of this sequence are the same as those of figure 4. In figure 5, the most evident change in the surface profile is that the first large capillary crest is initially small, but it is increasing in amplitude and

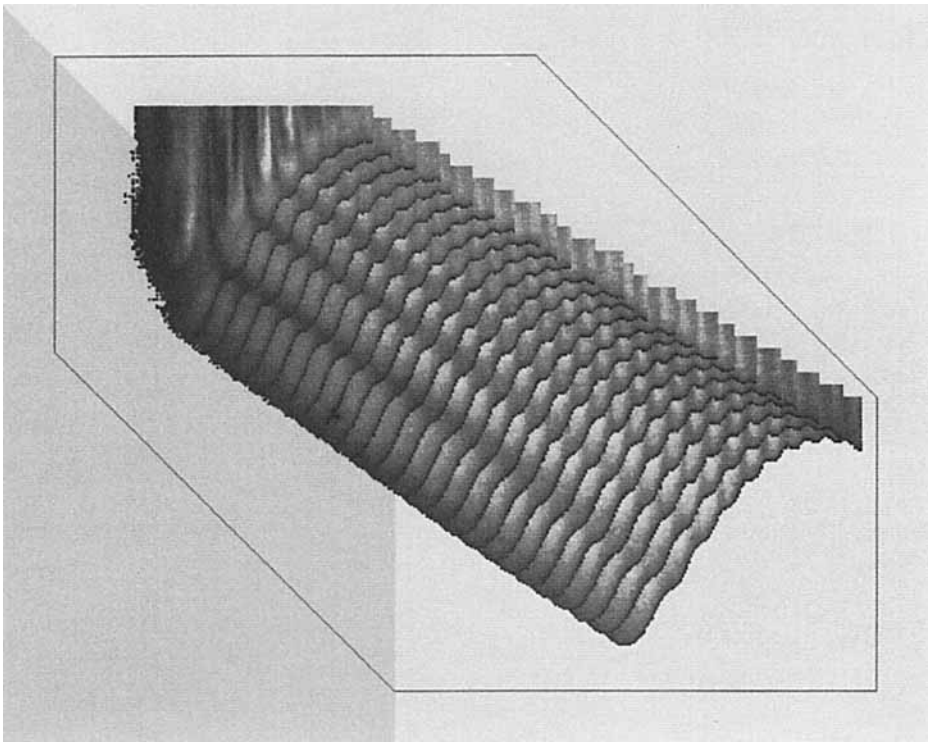

FIGURE 6. As figure 4 but the crest of the image in the foreground is located 2.5 wavelengths downstream of the wave maker.

reappearing in the later images. (In fact, in figure 6 which is three wavelengths downstream, it is seen that the first crest continues to recover and increase in amplitude.) Likewise, the second capillary wave is evolving. It is decreasing in amplitude and is nearly non-existent in the last image shown in figure 5. The cyclical process of decay and growth is similar to that which occurs in resonance phenomena. Two additional features seen in figure 5 are that the capillaries in and near the gravity-wave trough are quasi-stationary in the gravity-wave coordinate system and that these waves are growing and decaying, too. Also, it is seen that the average slope of the front face is decreased. Individual images of the entire wavelength show that the wave is more symmetric at larger distances from the wake maker. (For example, see figure 8.)

In figure 6, a time series is presented with the imaging system located three wavelengths downstream; otherwise, the set-up is the same as in figures 4 and 5. Now, the surface-wave profile is shaped beautifully and it is clear that the waves are stationary in the moving coordinate system. There is very little modulation of the wavelengths of the capillaries. The first two capillaries are decaying in space while the higher frequency capillaries appear to be stationary in amplitude and wavelength. Two additional time series are recorded four and five wavelengths downstream but are not presented. (Two individual frames from the last two stations' time series along with three other frames from the first three time series are presented in figure 9.) The most significant feature of these last two time series (not presented) is the systematic extinction of the capillaries, presumably by viscous effects.

In order to compare the experimental profiles with the theoretical solution of

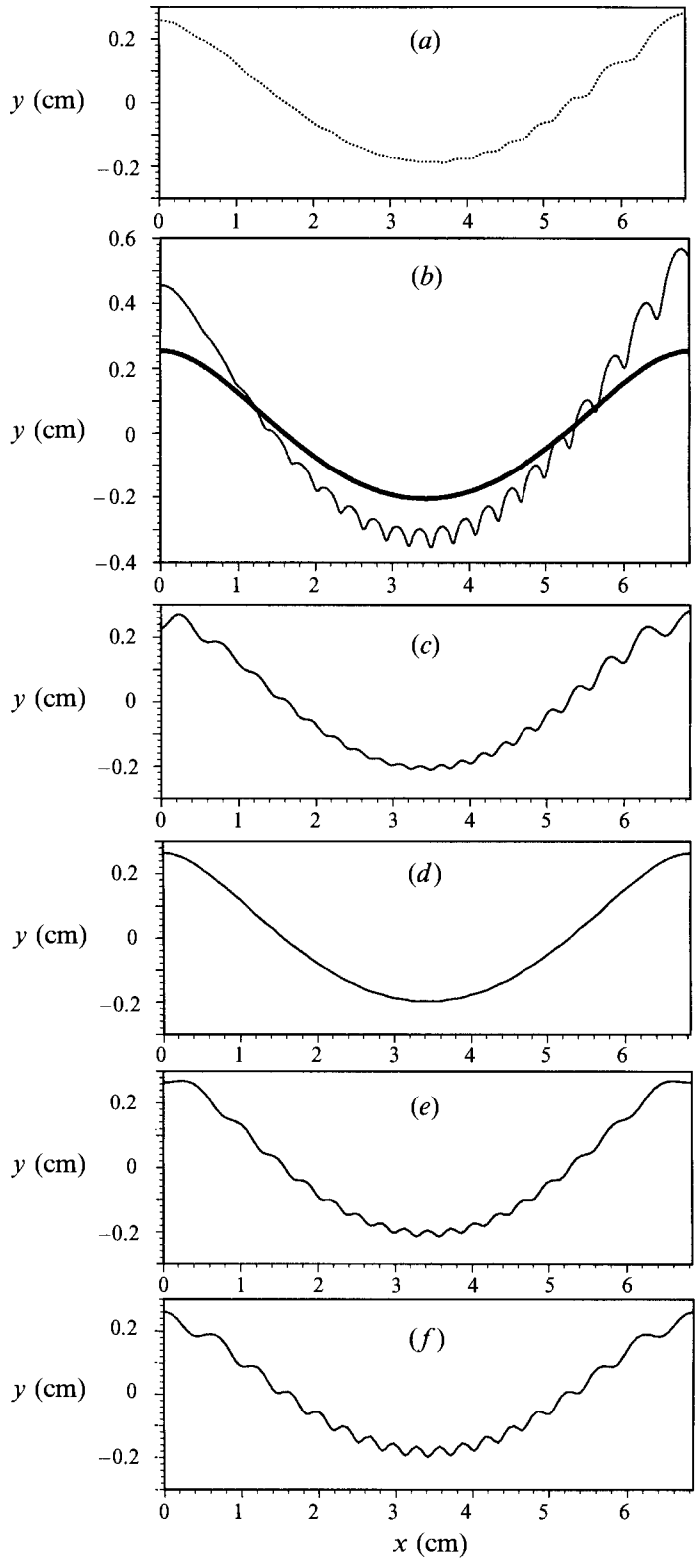

FIGURE 7. For caption see facing page.

Longuet-Higgins, an image is chosen arbitrarily from the imaging station located three wavelengths downstream (i.e. from the time series shown in figure 6). The first frame of this time series is chosen because the surface profile is quasi-stationary and nearly symmetric. Thus, the comparison between theory and experiment should be favourable. To calculate the Longuet-Higgins' solution, the wavelength and wave amplitude of the measure surface profile is used. As the amplitude of the experimental wavetrain is changing slowly in space, an average of the two sequential amplitudes in the image is used to calculate the amplitude to which the theory is matched. In the computations, the values of A and l are varied until the computed underlying gravity-wave wavelength and amplitude are identical with the measured wavelength and amplitude. For clarity in the comparisons of theory to measurements, the surface profile rather than the image is presented. To obtain this profile from the image, an edge-detection routine is implemented using the following spatial masks to compute the gradients in the x- and y-directions, respectively (see Gonzalez & Wintz 1987, p. 334):

$$\begin{matrix} -1 & -2 & -1 \\ 0 & 0 & 0 \\ 1 & 2 & 1 \end{matrix} \qquad \begin{matrix} -1 & 0 & 1 \\ -2 & 0 & 2 \\ -1 & 0 & 1 \end{matrix}.$$

Next, proceeding from the top of an image, column by column, the first pixel with gradient greater than 10 is chosen as an approximate location of the surface. Then, including 10 pixels above and below this pixel, the surface location is taken to be the pixel with the maximum gradient. (This *ad-hoc* technique, determined to be the best amongst many possibilities tested, is used to produce the measured profiles presented in figures 7 and 11. In each case, the surface profile determined in this manner is compared to the image to ensure duplication.) It is necessary here to discuss the subsurface portion of the image. Laser light entering the free surface is refracted and thus causes bright and dark regions to form beneath the surface. This is seen clearly in the front-most image in figure 4. Herein, no information from the subsurface portion of the images is used. (Figure 8 shows the subsurface more clearly.) The numeric search procedure used to determine the location of the surface (as shown in figures 7 and 11), and thus determine the waveform, treats each column of the image individually and searches from the top of the column downward until the maximum jump in light intensity is determined, thus locating the surface. Reiterating, the subsurface light-intensity gradients (which are also quite apparent in figure 10) do not influence the algorithm's location of the free surface.

As is seen in figures 7(*a*) and 7(*b*) where, for comparison, the vertical exaggeration is decreased by a factor of two, the measured and two of Longuet-Higgins' theoretical profiles are compared. The wave steepness and phase speed of the experimental wavetrain are 0.21 and 35.99 cm/s, respectively. (Typically, a wavetrain with this steepness is associated with weakly nonlinear theory. Experiments not reported show that the steepness of the wavetrain increases more slowly with increasing wave-maker stroke once the capillaries appear.) The theoretical profile with $A = 0.59$ and $l = 1.21$ predicts a smooth nonlinear, gravity waveform. The amplitudes of the parasitic capillaries are severely underpredicted. To determine the frequency of the theoretical parasitic waves, the value of A is increased until the amplitude of the capillary waves

FIGURE 7. Comparison of (*a*) the measured 5.26 Hz profile (the surface profile is located 2–3 wavelengths downstream) with (*b*) the theory of Longuet-Higgins (bold line $A = 0.59$, thin line $A = 0.90$); (*c*) the theory of Crapper; and (*d*), (*e*), and (*f*) three numerical solutions determined using the Schwartz & Vanden-Broeck scheme – convergent μ-values of 1.1165 (the 'natural' profile), 1.1204, and 1.1086, respectively.

in the theory are comparable to the measured ones. This profile is superimposed on figure 7(*b*). Clearly, once commensurate amplitudes are produced by increasing A to 0.9, the wavelengths of the theoretical capillaries are seen to be smaller than those measured experimentally.

The theoretical solution of Crapper, which uses the same solution for the underlying gravity wave as Longuet-Higgins but includes a different treatment of the capillary waves, is shown in figure 7(*c*). In order to compare to the crest-to-crest span of the gravity wave profile, as is done with the Longuet-Higgins theory, the theory of Crapper is computed as follows. Both theories are periodic; however, neither theory predicts an integral number of short waves riding on the gravity wave. Therefore, if calculations begin at a crest (trough), there is a discontinuity at the next crest (trough). Therefore, to obtain a continuous profile in the trough required for a crest-to-crest comparison, the Crapper theory, which begins in a trough, is calculated forward to the next crest and backward to the previous crest. This surface profile is shown in figure 7(*c*). It is seen that Crapper's theory predicts the same order-of-magnitude capillary-wave amplitudes on the forward face of the gravity wave as are measured experimentally; however, the theoretical amplitudes of the waves on the leeward face of the capillary wave are larger than the measured amplitudes. The wavelengths of the theoretical capillaries are smaller than those measured in the experiments. That is, both theories predict the capillary wavelengths to be less than those measured experimentally.

The three numerical solutions found using the boundary-integral formulation are presented in figures 7(*d*), 7(*e*), and 7(*f*). These three solutions have μ-values of 1.1165, 1.1204, and 1.1086, respectively. The steepness and surface-tension parameters, $(\epsilon, \kappa) = (0.06727, 0.06275)$, are those of the measured profile presented in figure 7(*a*). Although barely visible, about eight short waves are present on a half (crest-to-trough) wavelength shown in figure 7(*d*). Clearly, the short-wave amplitudes are overall much smaller than those seen in the physical experiments. This is the 'naturally' occurring waveform which, in the straightforward method described in §2, occurs in almost 96% of the solutions. The solution presented in figure 7(*e*) occurs in about 3% of the solutions and, in the vernacular of Schwartz & Vanden-Broeck, is a 'type 1' (capillary-type) wave as it has a dimple on the crest. On the other hand, the waveform presented in figure 7(*f*) is a 'type 2' (gravity-type) wave similar to the waveform shown in figure 10 of their publication. It occurs in about 1% of the straightforward calculations. The profiles shown in figures 7(*e*) and 7(*f*) have about 8.5 short waves present in a half (crest-to-trough) wavelength. Thus, these two solutions represent waveforms with an increasing number of short waves present as compared to the naturally occurring profile rather than a decreasing number as is seen in the experiments. That is, all numerically determined solutions contain short waves with larger wavenumbers than those measured experimentally. Figures 7(*e*) and 7(*f*) show short waves with amplitudes of the correct order of magnitude. No additional solutions are determined using the bootstrap method as described in §2. A surface profile that is similar in the number of short waves to that shown in figure 7(*a*) is not found.

The measured phase-speed parameter, $\mu = 1.2124$, gives an increase in phase speed of 8.6, 8.2, and 9.4% above the predicted values, respectively. Including additional phenomena which are neglected in the Schwartz & Vanden-Broeck formulation and are known to affect phase speed (e.g. viscosity, contamination, etc.) cause a decrease rather than an increase in phase speed. One possible explanation is that the numerical solution corresponding to the experiments is simply not found. A second possibility is that the slight distortion in the images (see figure 3) is sufficient to cause an error in c of approximately 4%. The numerical formulation is for a stationary, periodic

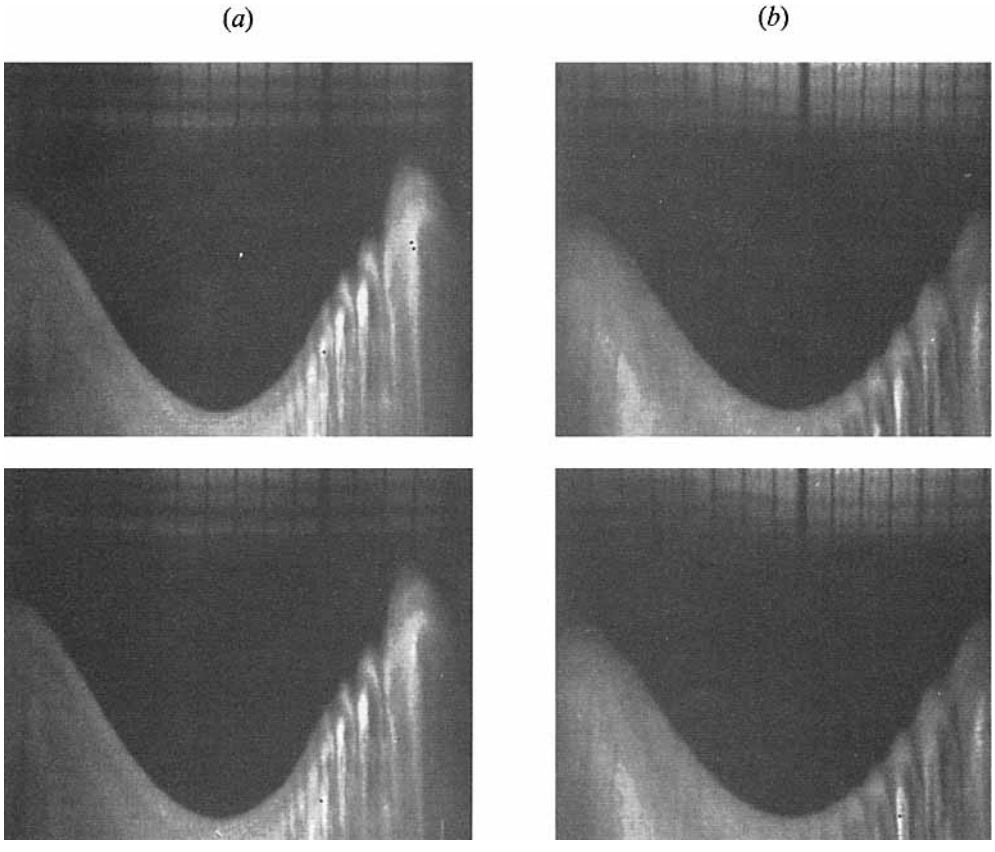

FIGURE 8. Two sets of images recorded 190 ms apart (5.26 Hz), (*a*) 7.1 cm and (*b*) 20.7 cm downstream. Clearly, the temporal periodicity of the wave fields is shown. The distances are measured from the wave maker to the image centres.

waveform in the moving coordinate system and thus there is no possibility of it predicting the evolution seen in the downstream direction in the experiments. A time-marching scheme such as developed by Huh (1991) is the minimum formulation required. As it is unknown whether the resonance-like processes seen in the physical experiments are related to viscous effects or not, it is unclear whether a time- or space-marching formulation of the inviscid problem can predict the profiles produced in the experiments, even neglecting the dissipation.

To facilitate the reconstruction of a wave field over several wavelengths of the gravity wave, a triggering technique is used. In §3, the triggering scheme is discussed. For the triggering technique to provide meaningful results, the wave field must be temporally periodic. Figure 8 shows two sets of images from the 5.26 Hz experiments recorded one temporal wave period (i.e. 190 frames apart at 1000 Hz recording rate) apart. Two spatial locations, 7.1 and 20.7 cm downstream of the wave maker, are shown. It is clear from these two sets of images that both the underlying gravity wave and the parasitic capillaries are temporally periodic regardless of the proximity of the measurement location to the wave maker. Thus, it is concluded that triggering the imager on the zero up-crossing of the wave-maker signal, at various overlapping imager locations, allows one to construct a mosaic of the surface profile.

A mosaic, composite image is presented in figure 9. It is produced using the zeroth

FIGURE 9. An 'extended' spatial series of the 5.26 Hz experiments showing 5 wavelengths of the wave field beginning 0.5 wavelengths downstream of the wave maker.

	First wavelength	Second wavelength	Third wavelength	Fourth wavelength	Fifth wavelength
$\overline{PE}_{non}$	1.153	0.815	0.841	0.916	0.831
$\overline{SE}_{non}$	1.645	1.128	1.119	0.987	0.880

TABLE 2. Computed values for non-dimensionalized average potential energy and surface energy for wavelengths shown in figure 9.

frames from each of the five imager positions of the 5.26 Hz experiments. At the top of each image, the scale used to provide redundant control of the horizontal placement of the images is visible. Wave propagation is from right to left. The first three downstream images correspond to the partial profiles show in the immediate foreground of figures 4, 5, and 6, respectively. In those figures, the dark portion of the image has been removed. In figure 9, the actual images are used to form the composite image. Using the composite image shown in figure 9, coordinates of the surface profile are obtained using the aforementioned surface location algorithm. From these data, the average potential energy per unit wavelength per unit crest width due to the presence of the wave, $\overline{PE}$, and the average surface energy per unit wavelength per unit crest width due to the presence of the wave, $\overline{SE}$, are calculated as a function of downstream position, x. The computations use the crest-to-crest gravity wavelength, L (defined as the distance between the maximum surface elevations), as the averaging distance. The equations used to calculate these quantities are

$$\overline{PE} = \frac{\rho g}{2L}\int_x^{x+L} y^2\,\mathrm{d}x \quad \text{and} \quad \overline{SE} = \frac{T}{L}\int_x^{x+L}\left[1+\left(\frac{\partial y}{\partial x}\right)^2\right]^{\frac{1}{2}} - 1\,\mathrm{d}x.$$

These quantities are non-dimensionalized by their corresponding linear-wave-theory values calculated for the same wave amplitude and length as measured one wavelength downstream and are denoted by $\overline{PE}_{non}$ and $\overline{SE}_{non}$. Table 2 presents the computed values for the five wavelengths shown in figure 9. In figure 9, it is seen that the parasitic capillary waves are generally decreasing in amplitude in the downstream direction; however, they are larger in the trough of the fifth image than in the trough of the fourth image. Apparently, energy exchange is still occurring. The data in table 2 show a decrease in surface energy in the downstream direction. This is in agreement with the qualitative conclusion. The potential energy is seen to be varying irregularly in the downstream direction. No explanation for this behaviour is known.

4.2. *The 4.21 Hz experiments*

Experiments are presented for steep gravity waves generated at 4.21 Hz. Many of the features exhibited by the 4.21 Hz wavetrain are similar to those of the 5.26 Hz wavetrain and are not presented. It is shown that the lower-frequency, steep gravity wave generates capillaries with higher wavenumbers. This is consistent with the theory

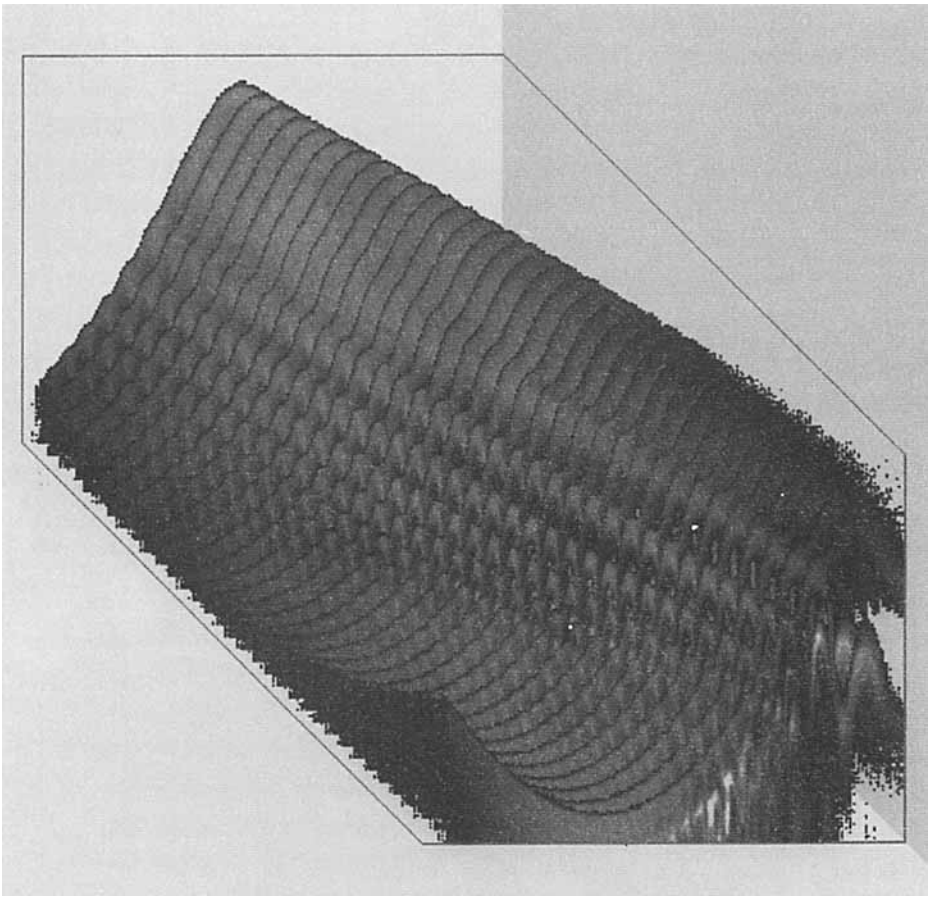

FIGURE 10. Time series of the 4.21 Hz wave profile showing about one-half wavelength of each image spaced 3 ms apart. The crest of the image in the foreground is located 1.5 wavelengths downstream of the wave maker.

and according to the theory is because the pressure disturbance due to the large crest curvature is travelling faster in the lower-frequency gravity wave. It is shown, too, that the capillary waves decay more rapidly in the 4.21 Hz experiments than in the 5.26 Hz experiments. This is consistent with the theory for free, gravity–capillary or capillary waves. It is shown, too, that the natural profile calculated numerically using the Schwartz & Vanden-Broeck formulation predicts amplitudes and wavenumbers of the short waves which are essentially not visible.

In figure 10, a time series of the crest-to-trough region of the 4.21 Hz gravity wave is shown. The centre of the imaging system is positioned approximately 1.5 linear wavelengths downstream and the portion of the series shown extends for about one-half wavelength. It is seen that the capillaries' positions are stationary features along the gravity wave (i.e. lines connecting the same phase on corresponding capillaries are at the same angle as a line connecting the crests of the gravity wave), with the uppermost (forward face of the crest region) capillaries' amplitudes decaying and the lowermost (trough region) capillaries' amplitudes modulating over time. As predicted by the theory, the wavelengths of the 4.21 Hz parasitic capillaries are less than those of the 5.26 Hz wavetrains. Presumably, this is due to the increase in phase speed of the

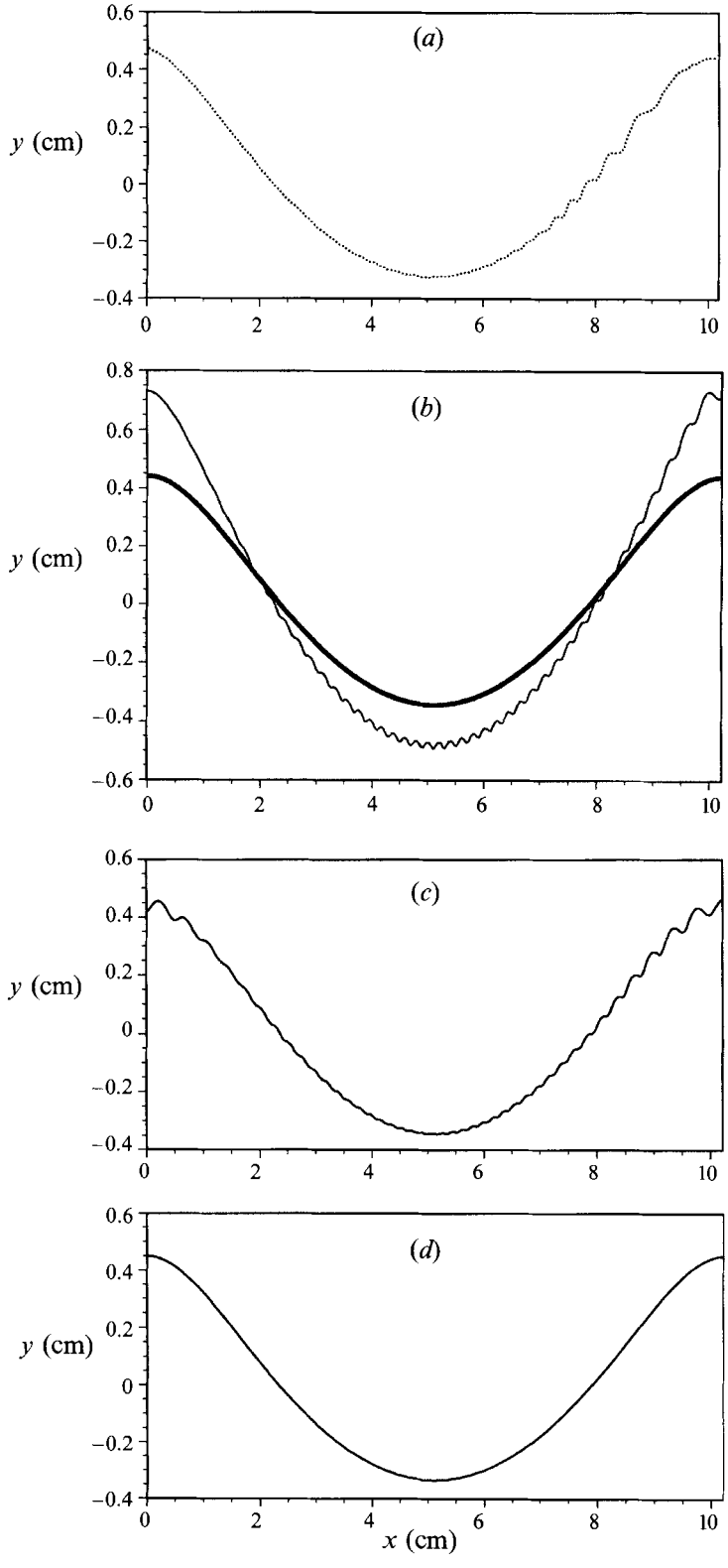

FIGURE 11. For caption see facing page.

lower-frequency gravity wave. Measured values are 43.03 and 35.99 cm/s, respectively. The phase speeds vary slightly in space. About 13 capillaries are present on the portion of the wave profile shown. In general, the wave profiles are very similar to those of the 5.26 Hz experiments.

The first frame, chosen arbitrarily from a time series recorded approximately two wavelengths downstream, is shown in figure 11(*a*) with the theory of Longuet-Higgins presented in figure 11(*b*). The experimental wavetrain is determined to have a wave steepness of 0.24 and a phase speed of 43.03 cm/s, where the amplitude is calculated by halving the average of the two crest-to-trough distances visible in the image. Again, the theoretical profile is obtained by matching the wave length and amplitude of the experiments to those of the theory (by altering A and l). In figure 11(*b*), the lower-steepness theoretical profile is shown for $A = 0.66$ and $l = 1.158$. Then, by increasing A until the capillaries' amplitudes are of the correct order of magnitude, a second theoretical profile is determined. A value of A of 0.9 is used. It is seen that the theory underpredicts the amplitudes and wavelengths of the parasitic waves if the measured wave steepness is used in the theory. Using a much steeper underlying gravity-wave profile predicts a reasonable value for the amplitude of the capillaries as compared to experiments, but the wavenumbers are still overpredicted.

Crapper's theoretical solution for the 4.21 Hz experiment is shown in figure 11(*c*). Consistent with the 5.26 Hz experiments, the theory predicts larger capillaries on the leeward face of the crest than are seen in the experiments. Also, the capillary wavelengths predicted by the theory are shorter than those that are recorded in the experiments.

In figure 11(*d*), the 'natural' profile for the 4.21 Hz case is presented. Clearly, the short-wave amplitudes are much smaller than those realized in the physical experiments, so small in fact that a comparison between predicted and measured numbers is not possible. The convergent value of μ, the phase-speed parameter, is 1.0923 a determined from the numerical solution, while the measured value is 1.1603. As in the 5.26 Hz experiments, the waveform is travelling at a phase speed greater than that predicted by the numerics. There is an increase in phase speed of about 6.2% in the experiment as compared to the numerics. A detailed search for additional profiles is not conducted.

As with the higher-frequency experiments, the 4.21 Hz waves exhibit temporal periodicity (at least when their steepness is restricted). Thus, using the triggering scheme, an extended composite profile is possible. In order to magnify the parasitic capillaries sufficiently, a vertical exaggeration of 7.8 is used (see table 1). This precludes recording a complete wavelength of the 4.21 Hz profile. Thus, five set-ups yield a composite profile which extends about 2.5 wavelengths. It is presented in figure 12. In general, the parasitic capillary waves are decaying with distance. The forward face of the wave profile 2–2.5 wavelengths downstream shows remnants of the parasitic capillaries through the focusing of the laser sheet beneath the water surface; however, the water surface is nearly smooth. This general decrease in surface energy is consistent with that seen in the 5.26 Hz experiments; however the lower-frequency gravity wavetrain experiences a more rapid decrease in the parasitic capillaries, which are almost non-existent by 2.5 wavelengths downstream.

FIGURE 11. Comparison of (*a*) the measured 4.21 Hz profile (the surface profile is located about 1.5–2.25 wavelengths downstream) with (*b*) the theory of Longuet-Higgins (bold line $A = 0.66$, thin line $A = 0.90$); (*c*) the theory of Crapper; and (*d*) the numerical solution determined using Schwartz & Vanden-Broeck's scheme – a convergent μ-value of 1.0923 (the 'natural' profile).

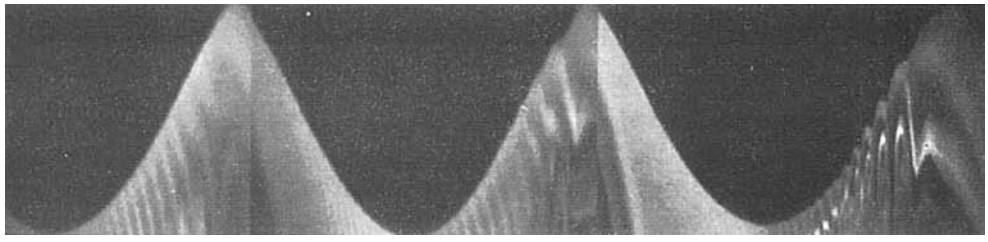

FIGURE 12. An 'extended' spatial series of the 4.21 Hz experiments showing about 2.5 wavelengths of the wave field beginning one wavelength downstream of the wave maker.

5. Conclusions

A new instrument and non-intrusive measurement technique is discussed. An intensified, high-speed video system is used to image surface profiles through magnifying optics. Owing to the disparate horizontal and vertical lengthscales inherent in water waves, a vertical exaggeration of about 8 is desirable for spatial measurement and is achieved through the use of cylindrical lenses. A longitudinal plane of fluid which includes the surface profile is illuminated using a laser sheet and a fluorescing dye. It is shown that this instrument is extremely accurate, with sufficient resolution to capture and quantify the capillary waves generated by steep, high-frequency gravity waves.

Several important similarities and differences are seen between theoretical and measured waveforms which evolve from large, single-frequency sinusoidal oscillations of a paddle which sits astride a uniform-depth channel. As predicted by theory, the wavelengths and amplitudes of the parasitic waves are decreasing in the downstream direction as measured in a coordinate system fixed to the crest of the gravity wave. The amplitude and wavelength of the capillaries are modulated in space, but they do not propagate with respect to the underlying wave. Thus, the parasitic capillaries are quasi-stationary with respect to a coordinate system fixed to the gravity wave.

Based on the steepness and phase speed of the experimental surface profile, it is seen that the Longuet-Higgins theory underpredicts the amplitude and lengths of the capillaries as measured in the experiments. Along the forward face of the surface profile, based on the steepness of the experimental wavetrain, Crapper's theory predicts the short-wave amplitudes reasonably well; however, it overpredicts the amplitudes along the leeward face. Crapper's theory underpredicts the lengths of the measured capillaries.

The 'natural' wave profiles predicted by the Schwartz & Vanden-Broeck formulation have short-wave amplitudes significantly smaller than the measured amplitudes, and in the case of the 5.26 Hz wavetrains, have wavenumbers larger than those measured. In the 4.21 Hz wavetrain, the numerically generated, natural amplitudes are so small that a comparison of wavenumbers is not possible. Three solutions, determined using two techniques, a straightforward method and a 'bootstrapping' method, are found in the case of the 5.26 Hz wavetrains. Aside from the natural profile, the other two solutions have wavenumbers larger than those measured experimentally; however, the amplitudes of the short waves are the correct order of magnitude. Recall that the experimental waveform presented in figure 7 is chosen arbitrarily from a time series of profiles, but its general features are similar to the other profiles. It is possible that the solution corresponding to the physical experiments simply is not found. As there is no known method for determining the number of solutions to the numerical formulation,

it is not known whether or not other solutions exist. Also, it is unknown whether the resonance-like processes seen in the physical experiments are related to viscous effects or not, and so it is unclear whether a time- or space-marching formulation of the inviscid problem can predict the profiles produced in the experiments, even neglecting the dissipation.

Estimates of the average surface energy due to the presence of the waves per unit wavelength per unit crest width show a decrease in the downstream direction. Estimates of the average potential energy per unit wavelength per unit crest width are seen to fluctuate downstream, partially due to the change in the waveform toward increased symmetry.

According to theory, steep, lower-frequency (4.21 Hz) gravity waves generate higher-wavenumber parasitic capillary waves than do steep, higher-frequency (5.26 Hz) gravity waves. In both cases, the crest curvature is assumed to increase the pressure locally; however, the lower-frequency gravity waves travel at higher phase speeds, thus generating larger-wavenumber parasitic capillaries. The experiments verify that higher wavenumbers are generated by the lower-frequency gravity wave, and, in addition, show that these shorter parasitic waves are dissipated more quickly than their 5.26 Hz counterparts. The parasitic capillaries generated by the 4.21 Hz gravity wave are barely visible about 2.5 wavelengths downstream while those generated by the 5.26 Hz gravity wave are seen five wavelengths downstream. Thus, the rapidity with which the higher-wavenumber capillaries are extinguished is in qualitative agreement with the viscous dissipation model for free, linear waves.

In future experiments, particle image velocimetry, if successful close to the surface, and if sufficient resolution is achieved, would facilitate the calculation of the average kinetic energy as a function of downstream location. Then, conclusions regarding energy dissipation are possible. A geometric-distortion correction could be implemented. To test whether the asymmetry seen in the experiments is an inviscid or viscous phenomenon, numerical calculations with the symmetry requirement removed are desirable, as are viscous calculations. Time- or space-marching calculations are required to predict the resonance-like behaviour seen in the physical experiments.

We wish to acknowledge and thank Professor W. W. Willmarth for the use of his laser. Our sincere appreciation is extended to Professor William W. Schultz for his useful comments as well as for the initial Schwartz & Vanden-Broeck numerical code which he generously gave us. This research was partially supported by the Office of Naval Research under an Accelerated Research Initiative, Contract No. N00014-91-J-1083 and partially supported by the Office of Naval Research under a University Research Initiative, Contract No. N00014-92-J-1650.

REFERENCES

CHANG, J. H., WAGNER, R. N. & YUEN, H. C. 1978 Measurement of high frequency capillary waves on steep gravity waves. *J. Fluid Mech.* **86**, 401–413.

CHEN, B. & SAFFMAN, P. G. 1979 Steady gravity–capillary waves on deep water – I. Weakly nonlinear waves. *Stud. Appl. Maths* **60**, 183–210.

CHEN, B. & SAFFMAN, P. G. 1980 Steady gravity–capillary waves on deep water – II. Numerical results for finite amplitude. *Stud. Appl. Maths* **62**, 95–111.

CHEN, B. & SAFFMAN, P. G. 1985 Three-dimensional stability and bifurcation of capillary and capillary waves on deep water. *Stud. Appl. Maths* **72**, 125–147.

COX, C. S. 1958 Measurement of slopes of high-frequency wind waves. *J. Mar. Res.* **16**, 199–225.

CRAPPER, G. D. 1957 An exact solution for progressive capillary waves. *J. Fluid Mech.* **2**, 532–540.

CRAPPER, G. D. 1970 Non-linear capillary waves generated by steep gravity waves. *J. Fluid Mech.* **40**, 149–159.

DAVIES, T. V. 1951 The theory of symmetrical gravity waves of finite amplitude. I. *Proc. R. Soc. Lond.* A **208**, 475–486.

GONZALEZ, R. C. & WINTZ, P. 1987 *Digital Image Processing*. Addison-Wesley.

HUH, J. 1991 A numerical study of capillary–gravity waves. PhD dissertation, Applied Mechanics, University of Michigan.

LONGUET-HIGGINS, M. S. 1963 The generation of capillary waves by steep gravity waves. *J. Fluid Mech.* **16**, 138–159.

LONGUET-HIGGINS, M. S. 1992 Capillary rollers and bores. *J. Fluid Mech.* **240**, 659–679.

MILLER, R. L. 1972 The role of surface tension in breaking waves. *Tech. Rep. Univ. Chicago*, no. 13, 1 October.

PERLIN, M. & TING, C.-L. 1992 Steep gravity–capillary waves within the internal resonance. *Phys. Fluids* A **4** (11), 2466–2478.

RUVINSKY, K. D., FELDSTEIN, F. I. & FREIDMAN, G. I. 1991 Numerical simulation of the quasi-stationary stage of ripple excitation by steep gravity–capillary waves. *J. Fluid Mech.* **230**, 339–353.

RUVINSKY, K. D. & FREIDMAN, G. I. 1981 The generation of capillary–gravity waves by steep gravity waves. *Izv. Atmos. Ocean Phys.* **17**, 548–553.

RUVSINKY, K. D. & FREIDMAN, G. I. 1985 Improvement of first Stokes method for the investigation of finite-amplitude potential gravity–capillary waves. In *IX All-Union Symp. on Diffraction and Propagation Waves, Tbilisi: Theses of Reports,* vol. 2, pp. 22–25.

SCHWARTZ, L. W. & VANDEN-BROECK, J.-M. 1979 Numerical solutions of the exact equations for capillary–gravity waves. *J. Fluid Mech.* **95**, 119–139.

YERMAKOV, S. A., RUVINSKY, K. D., SALASHIN, S. G. & FREIDMAN, G. I. 1986 Experimental investigations of the generation of capillary–gravity ripples by strongly nonlinear waves on the surface of a deep fluid. *Izv. Atmos. Ocean Phys.* **22**, 835–842.